

Interplay of Performance-Limiting Nanoscale Features in $\text{Cu}_2\text{ZnSn}(\text{S,Se})_4$ Solar Cells

Maurizio Ritzer,* Sven Schönherr, Philipp Schöppe, Gerardo Larramona, Christophe Choné, Galina Gurieva, Andreas Johannes, Konrad Ritter, Gema Martínez-Criado, Susan Schorr, Carsten Ronning, and Claudia S. Schnohr

Highly performing kesterite-based $\text{Cu}_2\text{ZnSn}(\text{S,Se})_4$ (CZTSSe) thin-film solar cells are typically produced under Cu-poor and Zn-rich synthesis conditions. However, these processing routes also facilitate the formation of secondary phases as well as deviations from stoichiometry, causing intrinsic point defects. Herein, the local composition of CZTSSe absorbers prepared with different nominal cation concentrations is investigated by applying energy dispersive X-ray spectroscopy and synchrotron X-ray fluorescence spectroscopy at the nanoscale to cross-sectional lamellae. The findings confirm the formation of ZnS(Se) secondary phases, whose presence, number, and dimension strongly increase with the reduction of the nominal Cu and increment of the nominal Zn content. Furthermore, the local compositions of the CZTSSe phase within the absorber reveal strong variations, leading to collateral and multiple off-stoichiometry types of the kesterite phase in the absorber, which cause different intrinsic point defects. Therefore, the off-stoichiometry type determined from the integral composition does not represent the complete true picture of this complex material system. Accordingly, the correlation of integral composition with electrical properties or conversion efficiency may be misleading. Overall, the approach provides new experimental insights into the nanoscale relationship among local compositional fluctuations, off-stoichiometry types, and secondary phases in these promising photovoltaic materials.

1. Introduction

The quaternary semiconductor material $\text{Cu}_2\text{ZnSn}(\text{S,Se})_4$ (CZTSSe), one of the so-called kesterites, has received great attention for thin-film solar cells owing to its direct, tunable bandgap energy between 1.0 and 1.5 eV,^[1] its high absorption coefficient,^[1,2] and its earth abundant, nontoxic constituents. Despite these ideal properties, the conversion efficiency is still limited to 12.6%,^[3] which is mainly attributed to losses in the open circuit voltage in relation to the optical bandgap. So far, the state-of-the-art absorbers are typically synthesized under Cu-poor and Zn-rich conditions,^[3–6] which are associated with favorable Cu vacancies and intrinsic p-type doping. However, these growth conditions also promote the formation of binary secondary phases,^[7–10] which can have detrimental effects on the device performance.^[11,12] In general, a discrepancy among the intended integral composition, typically probed via spatial global averaging, and the local elemental distribution in the actual CZTSSe absorber is produced by the presence of secondary phases.^[10,13]

M. Ritzer, Dr. S. Schönherr, Dr. P. Schöppe, K. Ritter, Prof. C. Ronning, Prof. C. S. Schnohr
Institut für Festkörperphysik
Friedrich-Schiller-Universität Jena
Max-Wien-Platz 1, Jena 07743, Germany
E-mail: maurizio.ritzer@uni-jena.de

Dr. G. Larramona, C. Choné
IMRA Europe S.A.S.
220 rue Albert Caquot, BP 213, Sophia Antipolis Cedex 06904, France

 The ORCID identification number(s) for the author(s) of this article can be found under <https://doi.org/10.1002/pssa.202000456>.

© 2020 The Authors. Published by Wiley-VCH GmbH. This is an open access article under the terms of the Creative Commons Attribution License, which permits use, distribution and reproduction in any medium, provided the original work is properly cited.

Correction added on 30 September 2020, after first online publication: Projekt Deal funding statement has been added.

DOI: 10.1002/pssa.202000456

Dr. G. Gurieva, Prof. S. Schorr
Abteilung Struktur und Dynamik von Energiematerialien
Helmholtz-Zentrum Berlin für Materialien und Energie
Hahn-Meitner-Platz 1, Berlin 14109, Germany

Dr. A. Johannes
European Synchrotron Radiation Facility (ESRF)
71 Avenue des Martyrs, Grenoble 38043, France

K. Ritter, Prof. C. S. Schnohr
Felix-Bloch-Institut für Festkörperphysik
Universität Leipzig
Linnéstraße 5, Leipzig 04103, Germany

Dr. G. Martínez-Criado
Growth and Properties of Heterostructures
Instituto de Ciencia de Materiales de Madrid (CSIC)
Cantoblanco, Madrid 28049, Spain

Prof. S. Schorr
Institut für Geologische Wissenschaften
Freie Universität Berlin
Malteserstr. 74–100, Berlin 12249, Germany

Such local compositional fluctuations are also inherently related to different intrinsic point defects and defect clusters that may significantly affect the device performance.^[11,14–18] It is, therefore, of particular interest to obtain detailed information about the nature, quantity, size, and spatial distribution of the secondary phases and the local composition of the quaternary material to further enhance the conversion efficiency.

Therefore, in this work, high-efficiency solar cell absorbers with different nominal compositions are examined by energy-dispersive X-ray spectroscopy (EDS) and high-spatial-resolution X-ray fluorescence analysis (nano-XRF). These techniques enable the detection, identification, and localization of secondary phases and off-stoichiometry types^[13,19–21] caused by local elemental fluctuations in CZTSSe solar cells. The EDS investigation shows that focusing on integral composition alone can be misleading by averaging away local fluctuations. These findings are corroborated by a 2D nano-XRF analysis. The investigation confirms the formation of ZnS(Se) secondary phases and reveals strong lateral variations of both the anion and cation distributions. Compositional modifications at selected grain boundaries are also found, which could influence the related solar cell performance.

2. Results and Discussion

2.1. Morphology and Elemental Distribution

Figure 1 shows the scanning electron microscopy (SEM) image and EDS maps (S, Se, Cu, Zn, and Sn) of the cross section of the as-prepared CZTSSe solar cell absorber of sample C1, which presents nominal Cu/(Zn + Sn), Zn/Sn, and Se/(S + Se) ratios of 0.83, 1.10, and 0.65, respectively. Not only the layered geometry of the sample is clearly visible by SEM and EDS, but also contrast variations within the absorber, small voids, and a thin Pt layer that was deposited to protect the absorber during the lamella preparation.^[22] The Mo back contact, onto which the

CZTSSe absorber was grown, is visible at the bottom of the SEM image (Figure 1a) and seems to be also present in the S map (Figure 1b). However, the alleged S signal in the Mo layer actually originates from the Mo L_α lines, which strongly overlap with the S K_α lines (see Figure S2, Supporting Information). A thin Mo–Cu–(S,Se) layer is observed between Mo and CZTSSe. In the literature, Cu diffusion into the Mo(S,Se) layer during the lamella preparation has been reported;^[23,24] however, the high Cu concentration detected here is of about 14 at% points rather than the formation of a Mo–Cu–(S,Se) compound during the absorber synthesis. The kesterite absorber features small voids with the lateral sizes up to few 100 nm both within the absorber layer and at the interface between the Mo–Cu–(S,Se) and CZTSSe. Furthermore, the most prominent characteristics are small spots ranging between 200 and 650 nm size with a composition different from CZTSSe. They seem to be Zn- and S-rich, whereas Cu, Se, and Sn appear to be absent or strongly reduced, indicating the formation of secondary phase segregations. Two different phases might be formed, namely, ZnS(Se) or Zn(Cu,Sn)S(Se). X-ray diffraction data^[25] taken on similarly produced absorbers showed only the presence of ZnS(Se) secondary phases. Furthermore, X-ray absorption near-edge structure spectroscopy^[26] measurements on absorbers prepared by physical vapor deposition co-evaporation corroborate the findings. Segregations of ZnS(Se) were also found for CZTSSe thin films prepared by a non-toxic solvent-based process using transmission electron microscope (TEM)-EDS.^[27] Thus, we assume the formation of ZnS(Se). The presence of Cu and Sn signals is not contradictory, because the composition is averaged along the beam direction over the lamella thickness of 170 nm. Therefore, secondary phases can be detected as a superposition together with CZTSSe. In the investigated area, the number and size of these secondary phase segregations appear to be larger close to or at the absorber surface; however, several segregations within the absorber and close to the back contact can also be

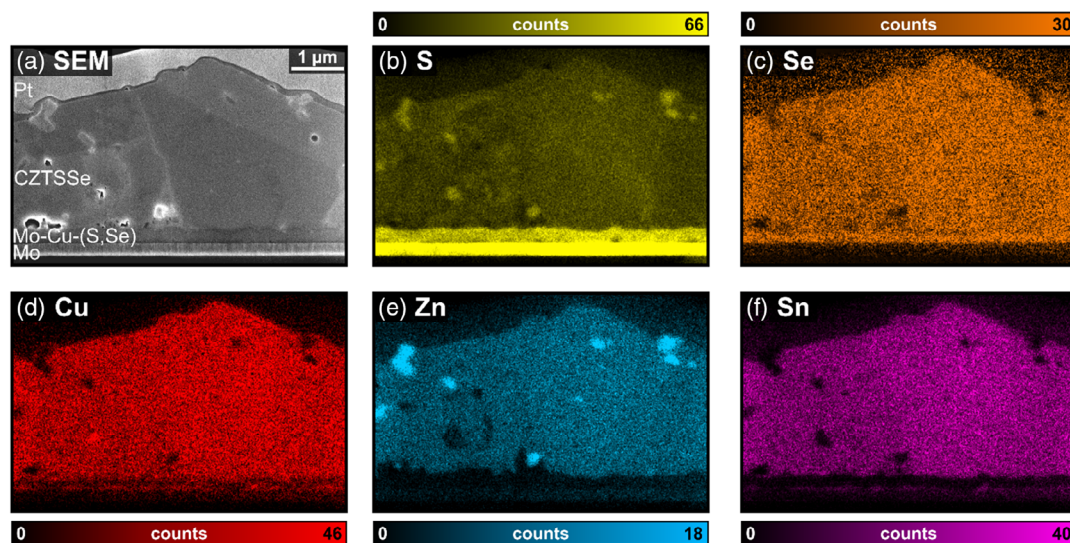


Figure 1. a) SEM image and b–f) EDS intensity maps for the five absorber elements of the lamella taken out of a CZTSSe absorber with a nominal Cu/(Zn + Sn) ratio of 0.83, a nominal Zn/Sn ratio of 1.10, and a nominal Se/(S + Se) ratio of 0.65 (C1). The alleged S signal in the Mo layer actually originates from Mo L_α lines, which strongly overlap with the S K_α lines. The lamella thickness was about 170 nm.

identified. Among the different possible secondary phases, ZnS is believed to be the least detrimental due to its semiconducting nature combined with a wide bandgap around 3.91 eV.^[26,28] Nevertheless, Just et al. reported a reduced current density, fill factor, and open circuit voltage, and, therefore, adverse effects on the electronic properties caused by ZnS.^[26]

2.2. Evaluation of the Spatially Resolved Composition and Off-Stoichiometry Types

From Figure 1d–f, except for the secondary phases, the cation distributions in the absorber seem to be fairly homogeneous. In contrast, variations in the S and Se maps are observed in good agreement with previous studies.^[18,29] To investigate such spatial heterogeneity in more detail and to compare the nominal to the actual absorber composition, 20 selected areas of $200 \times 200 \text{ nm}^2$ dimensions were defined on the absorber without any secondary phases. Their respective EDS spectra were analyzed in detail by AZtec. As the estimated concentrations depend on different parameters, such as transition probabilities, detector efficiency, and corrected background, the lamella prepared from the homogeneous, stoichiometric, single-phase $\text{Cu}_2\text{ZnSnSe}_4$ (CZTSe) reference was used for calibration. As this lamella did not contain S, only the cation contents were calibrated. The average atomic concentrations, namely, the mean value and standard deviation of the 20 spots, for both reference and C1 samples are listed in

Table S1, Supporting Information (rows 1 and 2, see Supporting Information). The statistical standard deviation of the homogeneous reference sample was used to define the experimental uncertainty: about $\pm 2\%$ (relative) with respect to the cation atomic percent and approximately $\pm 3\%$ with respect to the $\text{Cu}/(\text{Zn} + \text{Sn})$ and Zn/Sn cation ratios (see Table S2, Supporting Information).

The observed data fluctuations for C1 are much larger than those for the CZTSe reference, suggesting actual spatial variations of the local CZTSe composition. Especially, the S and Se concentrations exhibit pronounced deviations, which agree well with earlier studies.^[18,29] To investigate the cation variations in detail, **Figure 2** plots the Zn/Sn ratio as a function of the $\text{Cu}/(\text{Zn} + \text{Sn})$ ratio for the randomly chosen 20 individual spots (orange circles), the average of these 20 values (red circle) with the corresponding standard deviations as error bars (see Table S2, Supporting Information), and the nominal composition (black star). The dark gray area corresponds to one standard deviation, and the light gray area corresponds to two standard deviations obtained from the measurement of the stoichiometric CZTSe reference. In the following, the plot for each sample will be analyzed separately.

In Figure 2a, in agreement with the calibration procedure, the average composition reflects the stoichiometry of the reference material ($\text{Cu}/(\text{Zn} + \text{Sn}) = 1.00$ and $\text{Zn}/\text{Sn} = 1.00$), whereas the 20 individual spots are randomly distributed within the experimental accuracy around this composition. Assuming the reference sample to be homogeneous, and also assuming a

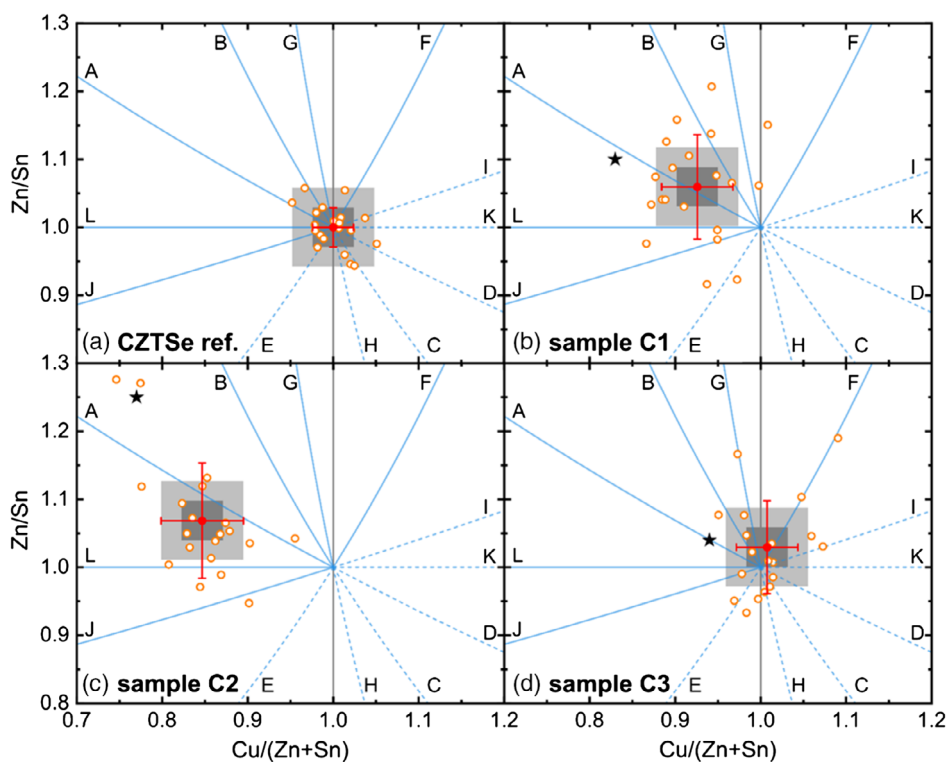


Figure 2. Calibrated cation ratio plots for the stoichiometric CZTSe a) reference and the three different CZTSe samples C1–C3. b–d) All off-stoichiometry types (A–L)^[13,19–21] are shown by solid and dashed blue lines. The nominal composition is marked by a black star. The local compositions of the 20 individual spots are given as orange circles, whereas the average of these values is given as red full circle with the corresponding standard deviations as error bars. The dark grey area corresponds to one standard deviation, and the light grey area corresponds to two standard deviations obtained for the measurement of the stoichiometric reference. For samples C1–C3, these deviations are used as the experimental uncertainty and are depicted with respect to the average value.

Gaussian distribution of data points, the graph can be used to distinguish between experimental uncertainty and real compositional variations. The errors bars (± 0.03 for both Cu/(Zn + Sn) and Zn/Sn) correspond to one standard deviation and span the dark gray area, containing 68% of the data points, whereas the light gray area represents two times the standard deviation, including 95% of the data. If the variation of the 20 individual data points for the CZTSSe absorber clearly exceeds these statistical deviations, then real fluctuations of the local CZTSSe compositional can be considered.

Figure 2b shows the calibrated cation ratio plot for C1, which is also presented in Figure 1. The average composition indeed reveals Cu-poor and Zn-rich conditions (Cu/(Zn + Sn) = 0.92 and Zn/Sn = 1.05). Compared with the nominal composition (Cu/(Zn + Sn) = 0.83 and Zn/Sn = 1.10, black star) and considering the experimental uncertainty—one or two standard deviations—there is a clear discrepancy between nominal and measured average quantities; i.e., the CZTSSe absorber layer is, on average, less Cu-poor and less Zn-rich than the nominal values. The fact that the average CZTSSe composition is still Cu-poor, Zn-rich demonstrates the possibility to grow off-stoichiometric Zn-rich kesterite (Zn/Sn > 1) by this deposition method. Previously, Just et al.^[9] reported that the Zn/Sn ratio is constrained to 1 for both Cu₂ZnSnS₄ (CZTS) and CZTSe grown under Zn-rich conditions but in a co-evaporation process. This might indicate that the achievable range of off-stoichiometry differs for different synthesis routes. In fact, various types of off-stoichiometric CZTS and CZTSe powders were grown by solid-state reaction, including Cu-poor, Zn-rich material.^[10,19,20] In the present case, the occurrence of ZnS(Se) secondary phase segregations leads to a less Cu-poor, Zn-rich average CZTSSe composition than expected, although the absorber material is still, on average, Cu-poor, Zn-rich, and thus off-stoichiometric. With respect to the 20 individual spots, the variation of the data points is much larger than that for the stoichiometric reference (Figure 2a). Accordingly, the standard deviations ($\sigma(\text{Cu}/(\text{Zn} + \text{Sn})) = 0.04$ and $\sigma(\text{Zn}/\text{Sn}) = 0.08$) are significantly higher than for the reference (shown in Figure 2b as dark gray area). In fact, for the Zn/Sn ratio, the standard deviation is more than twice the standard deviation of the CZTSe reference (light gray area). This finding proves the presence of real spatial fluctuations in the local composition of the CZTSSe absorber.

In general, variations of the cation concentrations are connected to several kinds of off-stoichiometry types (referred to as A–L)^[13,19–21] that have been proposed based on different cation substitution reactions, assuming charge balance and unchanging valence states.^[21] To classify the absorber and the observed fluctuations, the off-stoichiometry types are also shown in Figure 2 as dotted and straight blue lines. Similar to the nominal composition, the average absorber composition can be assigned to the A-type featuring Cu vacancies V_{Cu} and Zn_{Cu} anti-sites,^[21] which form a shallow acceptor and donor level, respectively, and result in the beneficial overall p-type conductivity.^[14] However, the presence of real spatial fluctuations indicates domains that do not correspond to the A-type. Instead, the CZTSSe absorber features local contributions from a wide range of off-stoichiometry types, including A, B, E, G, J, and L. While the A-type leads to the beneficial p-type conductivity, the other defect types feature Zn_{Sn}, Zn_{Cu}, and Sn_{Cu} anti-sites, V_{Cu} and V_{Zn} vacancies, and Zn_i

interstitials.^[13,19,20] Some of these defects form deep donor and acceptor states, which might act as electron recombination centers, reducing the conversion efficiency.^[14]

The same evaluation was performed for the two other lamellae prepared out of absorbers, which were synthesized under the same growth conditions but with different nominal compositions: one even more Cu-poor, Zn-rich (C2) and a second one close to the CZTSSe stoichiometry (C3). The nominal Se/(S + Se) ratio of 0.65 stayed the same for all three samples.

Figure 2c shows the calibrated cation ratio plot for C2. Similar to C1, the average composition evaluated by EDS shows deviations from the nominal value (Cu/(Zn + Sn) = 0.77 and Zn/Sn = 1.25), also revealing a less Cu-poor and less Zn-rich absorber with Cu/(Zn + Sn) = 0.85 and Zn/Sn = 1.07. Compared with C1, this deviation is quite similar to the Cu/(Zn + Sn) ratio, but even higher for the Zn/Sn ratio. The latter can be explained by the formation of even more and larger ZnS(Se) secondary phase segregations with the sizes up to more than 1 μm (for EDS intensity maps, see Figure S3, Supporting Information). The average absorber composition corresponds to a mixture of A and L off-stoichiometry types. The error bars representing one standard deviation of the 20 individual spots ($\sigma(\text{Cu}/(\text{Zn} + \text{Sn})) = 0.05$ and $\sigma(\text{Zn}/\text{Sn}) = 0.08$, similar to C1) fully encompass the corresponding A- and L-type lines, and most of the 20 individual compositions can be classified as A- or L-type or as a mixture of both. Thus, the beneficial V_{Cu} vacancies of the A-type compete against the harmful Sn_{Cu} anti-sites of the L-type,^[20] which form deep donor states in the bandgap.^[14] One spot even reveals a composition of the J-type, which also forms a detrimental deep donor state, namely, Sn_{Cu}.^[14,20]

Finally, Figure 2d displays the calibrated cation ratio plot for C3. The nominal composition of C3 (Cu/(Zn + Sn) = 0.94 and Zn/Sn = 1.04) is close to stoichiometry, and the evaluated average composition is even closer to this point with Cu/(Zn + Sn) = 1.00 and Zn/Sn = 1.03. Thus, sample C3 shows the smallest deviation between nominal and evaluated average values, in excellent agreement with the fact that hardly any ZnS(Se) secondary phase segregations were observed for this composition (for EDS intensity maps, see Figure S4, Supporting Information). Accordingly, ZnS(Se) secondary phase segregations seem to be formed only if the Zn concentration exceeds a critical value, and/or the Cu concentration falls below a critical amount. Just et al. proposed a critical value for the Zn/Sn ratio of ≈ 1.09 ,^[9] which is consistent with our findings. The average CZTSSe composition is close to stoichiometry, and therefore, no off-stoichiometry type would be assigned to this sample. However, the standard deviations ($\sigma(\text{Cu}/(\text{Zn} + \text{Sn})) = 0.04$ and $\sigma(\text{Zn}/\text{Sn}) = 0.07$) are again significantly larger than the ones for the CZTSe reference, demonstrating that all three CZTSSe absorbers feature real spatial fluctuations in the local kesterite composition. For C3, this corresponds to the presence of different off-stoichiometry types, even if the average composition is close to stoichiometry. Thus, it turns out that some of the individual spots show compositions associated with harmful Cu-poor off-stoichiometry types, namely, the B-, E-, and G-type, whereas others constitute Cu-rich off-stoichiometry types, such as the F- and I-type. The latter features Zn_{Sn} and Cu_{Sn} anti-sites and Cu_i and Zn_i interstitials,^[19,20] which also form deep donor and acceptor levels.^[14] The absence of A-type defects presumably leads to

insufficient intrinsic doping and, thus, to a reduced p-type conductivity. Both effects are expected to limit the conversion efficiency of a device made from such a CZTSSe absorber.

2.3. Correlation of the Intrinsic Properties with the Conversion Efficiency

Indeed, these intrinsic properties of the absorber correlate with the conversion efficiency of complete solar cells, which were produced under the same synthesis conditions and with the same nominal composition (see Figure S5, Supporting Information). Despite the formation of many and large ZnS(Se) secondary phase segregations as well as mixture of A and L off-stoichiometry types, composition C2 yields the highest conversion efficiency, indicating that these secondary phases are not the main limitation in CZTSSe at the current performance level. Compared with C1, the increased efficiency might be explained by a smaller amount of different off-stoichiometry types. Finally, C3 achieved the lowest conversion efficiency even though the absorber is free of secondary phases. However, this material does not contain beneficial A-type defects, which probably causes insufficient doping. Instead, several types of harmful deep defects are most likely present, potentially acting as electron traps. These results unambiguously show the risk associated with deducing the off-stoichiometry type from the integral composition alone. Moreover, the need of Cu-poor and Zn-rich conditions becomes apparent, leading to less harmful defects and improved intrinsic doping. By combining favorable off-stoichiometry types with a potential suppression of ZnS(Se) secondary phase segregations, a further enhancement of the conversion efficiency might be achievable.

2.4. Imaging of Nanoscale Compositional Fluctuations and Variations at Grain Boundaries

Figure 3 shows the SEM image of the cross section of the same lamella (as shown in Figure 1) but from a slightly different area together with the nano-XRF maps. The use of a hard X-ray nano-beam for compositional analysis not only improves the elemental sensitivity at higher energies but also the detection limits, allowing the determination of much lower compositional variations at nanometer scale, such as variations located at grain boundaries^[30–32] or nanoscale secondary phases.^[13,30] The only drawback is that S cannot be detected and quantified, because the experimental setup was under ambient conditions with a significant low-Z absorption by the air and the detector Be window. In a pixel-by-pixel basis, the fitting of individual nano-XRF spectra using the PyMCA code^[33] allows the generation of elemental maps. Figure 3b–f displays the integrated XRF counts for Mo and the detectable absorber elements (Se, Cu, Zn, and Sn). The same layered geometry is discernible, consisting of the Mo–Cu–(S,Se) layer followed by the CZTSSe absorber and the Pt layer. The XRF intensity maps show the same elemental characteristics as the EDS measurements but with more details. The formation of Zn hot spots correlates with a depletion or absence for all other elements, which validates the assumption of ZnS(Se) secondary phase segregations. Moreover, the Se pattern shows strong spatial fluctuations.

During the XRF acquisitions, the nickel grid onto which the lamella was mounted slightly attenuated the XRF radiation and, therefore, influenced the absolute values. As this attenuation was homogeneous throughout the entire lamella, relative changes between different areas on the absorber are still reliable. Therefore, maps of the relative differences of the cation ratios,

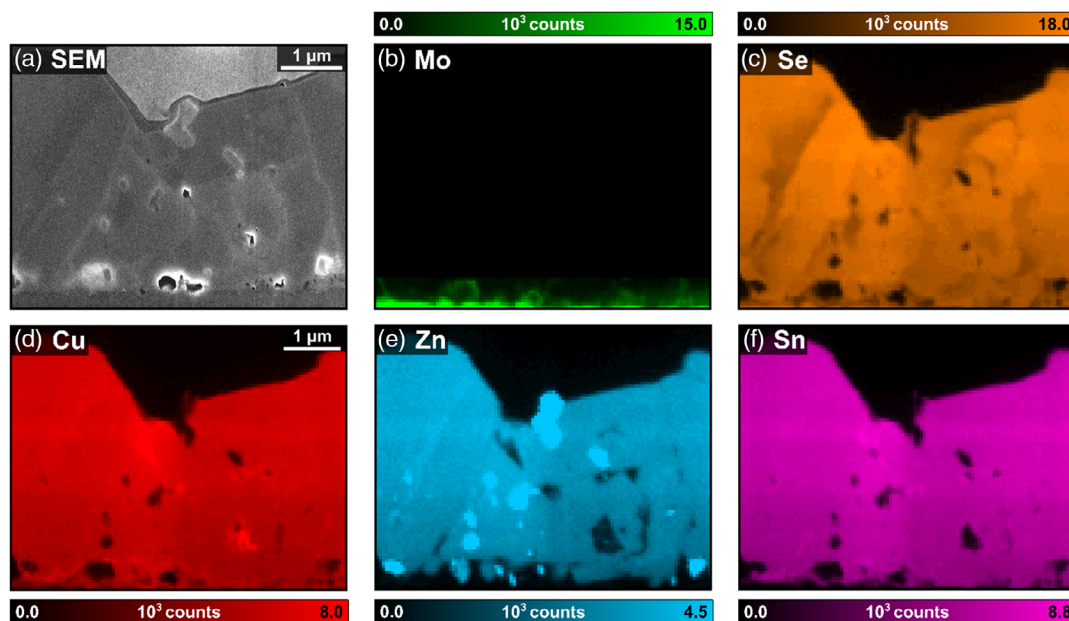


Figure 3. a) SEM image and b–f) fitted nano-XRF intensity maps for Mo and the four detectable absorber elements, measured on the same lamella, as shown in Figure 1 (sample C1), but from a slightly different area. The intensity maps were obtained by fitting the corresponding spectrum for each pixel individually with PyMCA³⁵ and showing the integrated counts for each element for each pixel. The Mo present in the voids is an artefact from the lamella preparation. A representation of the same data using a “false color” scheme is shown in Figure S6, Supporting Information.

named $\Delta(\text{Cu}/(\text{Zn} + \text{Sn}))$ and $\Delta(\text{Zn}/\text{Sn})$, were calculated by determining the mean value of the cation ratio similar to the EDS measurements, i.e., from 20 spots with an area of $200 \times 200 \text{ nm}^2$ each and without secondary phases. This mean value was then subtracted from the local value for every pixel. As a reference for the uncertainty, the same stoichiometric lamella used for EDS was also investigated by nano-XRF. **Figure 4** displays all the resulting subtraction maps of the cation ratios for all samples C1–C3 as well as for the CZTSe reference (see Figure S9, Supporting Information, for SEM images of the absorbers). The latter reveals a homogeneous distribution, where the noise represents the experimental uncertainty. Compared with the EDS data, the standard deviation for the cation ratios obtained for 20 individual spots is decreased to 0.01 for $\text{Cu}/(\text{Zn} + \text{Sn})$ and 0.02 Zn/Sn , which reflects a higher sensitivity by roughly a factor of 2 (compare Table S2 and S3, Supporting Information). Note that for a single pixel, the uncertainty is increased to 0.04 for $\text{Cu}/(\text{Zn} + \text{Sn})$ and 0.05 Zn/Sn due to lower counting statistics.

Figure 4c,d exhibits the $\text{ZnS}(\text{Se})$ secondary phase segregations for C1 with a strong anti-correlation behavior: regions with an increase in the Zn/Sn ratio present a substantial reduction in the $\text{Cu}/(\text{Zn} + \text{Sn})$ ratio. Sample areas without absorber are colored by a light gray in these maps. In Figure 4d, the most prominent new feature, compared with the XRF intensity maps shown in Figure 3, is a clear contrast between the left and right sides in the $\Delta(\text{Zn}/\text{Sn})$ map. This finding validates the spatial fluctuations of the local CZTSSe composition deduced from Figure 2b and the corresponding formation of local domains associated with various off-stoichiometry types. Interestingly, the $\Delta(\text{Cu}/(\text{Zn} + \text{Sn}))$ map does not show such a disparity, indicating that for this particular case, spatial fluctuation mostly concerns the Zn and Sn distributions (see also Figure S7, Supporting Information), as already indicated by the smaller standard deviation of the $\text{Cu}/(\text{Zn} + \text{Sn})$ ratio compared with

the Zn/Sn ratio in Figure 2b. Nevertheless, both maps for C1 also disclose domains with an increased Cu and a decreased Zn content, whereas the Sn concentration is unchanged or slightly increased (see also Figure S7, Supporting Information). The size of both domains and secondary phases strongly differs and decreases down to the resolution limit of the synchrotron nanobeam (see black circles and Figure S8, Supporting Information). On top of the Mo-Cu-(S,Se) , a layer featuring similar conditions with an increased $\text{Cu}/(\text{Zn} + \text{Sn})$ ratio and a decreased Zn/Sn ratio is apparent. A closer examination of these deviations reveals variations larger than 0.05 for both cation ratios, excluding an explanation based on the experimental uncertainty. As a result, these less Cu-poor and less Zn-rich regions represent real compositional fluctuations, suggesting a spatial variation of the p-type conductivity caused by a reduced number of V_{Cu} vacancies. The same quantitative evaluation, as shown in Figure 4, was not possible by EDS analysis because of the low statistics at similar spatial resolution. Relative maps can be calculated only at about $200 \times 200 \text{ nm}^2$ resolution, for which small features are averaged out.

Using high-angle annular dark-field scanning transmission electron microscopy (HAADF-STEM), the grain boundaries of the absorber have been identified (see Figure S8b, Supporting Information). By comparing with Figure 4c,d (black arrow), it becomes evident that selected grain boundaries exhibit a less Cu-poor and less Zn-rich composition, whereas Sn shows no obvious trend (see also Figure S7, Supporting Information). The size of the grain boundary (1–2 nm) is much smaller than the X-ray beam dimension (about 50 nm), so that compositional variation at the grain boundary is likely to be much larger. Similar Cu enrichments at grain boundaries and their likely detrimental effects were already observed for pure selenide and sulfide absorbers by EDS in a TEM^[24,34] and by atom probe tomography.^[35] The Cu enrichment likely reduces the amount of Cu vacancies V_{Cu} and may even promote the formation of

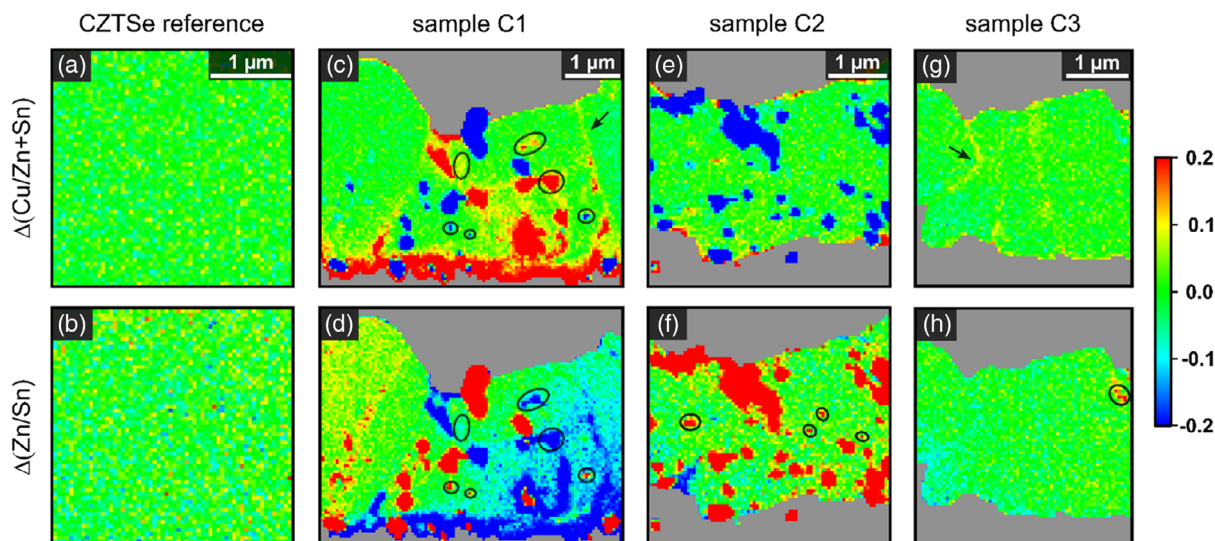


Figure 4. Deviation of the cation ratio from the respective mean value for $\text{Cu}/(\text{Zn} + \text{Sn})$ and Zn/Sn , namely, $\Delta(\text{Cu}/(\text{Zn} + \text{Sn}))$ and $\Delta(\text{Zn}/\text{Sn})$, for the CZTSe reference lamella and the three different samples C1–C3. They are calculated by subtracting the mean value of the ratio for the absorber region of a given map from the actual value of that particular pixel. Black circles mark new small features, and black arrows point to grain boundaries with a changed composition. The grey regions mark the areas where no absorber was present, i.e., voids, the Mo back contact, the Mo-Cu-(S,Se) layer, Pt, or air.

detrimental Cu_{Zn} anti-site defects, thus enhancing the carrier recombination.^[36,37] Moreover, the literature also reports Zn^[35] and Sn-enriched^[38] grain boundaries, which were not observed in the present case. Along the less Cu-poor grain boundaries, additional small less Cu-poor domains agglomerate, where the Cu/(Zn + Sn) ratio increases by up to 0.15 while the Zn/Sn ratio decreases by a similar quantity. As parts of the absorber seem to be quite homogeneous, line scans were performed in the vertical and horizontal directions to further evaluate this tendency (see Figure S10 and S11, Supporting Information). In the vertical direction, no gradients are revealed, whereas a slope in the Zn/Sn ratio is clearly present in the horizontal direction.

For C2, we observe the same secondary phase segregations as by EDS, but some even smaller features become also visible (see black circles in Figure 4f). Compared with C1, no less Cu-poor region at the back contact is formed. Moreover, there are no variations at grain boundaries or compositional gradients (see also Figure S10 and S11, Supporting Information). In contrast, for C3, there are no secondary phases (which was already discussed earlier for the EDS analysis), no less Cu-poor layer at the back contact, and no compositional gradients (see also Figure S10 and S11, Supporting Information). We observe an increase in the Zn/Sn ratio in the upper right area of the absorber (see black circle in Figure 4h). However, we did not assign this increase to a ZnS(Se) secondary phase, because the Zn/Sn ratio is only slightly higher (roughly 0.12) than for the surrounding CZTSSe material. On the other hand, we observe an increased Cu concentration accompanied by a slightly decreased Zn concentration and an unchanged Sn concentration for selected grain boundaries (black arrow in Figure 4g).

2.5. Summary of Compositional Variations for Six Different Lamellae

To get better statistics, the evaluation of the elemental distribution was performed on two lamellae from different positions of the sample (called I and II) for all three compositions. The results are summarized in **Table 1**, addressing the formation of secondary phase segregations, compositional fluctuations of the CZTSSe absorber, compositional variations at grain boundaries, and elemental changes close to and at the back contact.

For C1 and C2, both lamellae showed the formation of ZnS(Se) secondary phase segregations in varying amounts, whereas no secondary phases were observed for C3. The number and size of ZnS(Se) segregations, thus, clearly increase with decreasing nominal Cu/(Zn + Sn) and increasing nominal Zn/Sn ratio. Surprisingly, we also observed elemental Cu secondary phase segregation, but only for lamella C1-II. Apart from the secondary phase segregations, the absorber homogeneity depends on the nominal composition and on the position within the CZTSSe layer. For C3, no compositional gradients are observed, but for C2-II, a vertical gradient is visible, whereas a horizontal gradient is present for C1-I. Another difference is observed for the presence of selected grain boundaries with varied composition, which occur for both lamellae of C1 and C3 but not for C2. These grain boundaries are less Cu-poor, less Zn-rich, whereas the Sn composition is mostly unchanged. A less Cu-poor, less Zn-rich region close to the back contact

Table 1. Summary of the observed compositional variations for the six investigated lamellae with the three different compositions C1–C3.

| Composition | C2 | | C1 | | C3 | |
|--|------|----|------|----|------|----|
| Nominal Cu/(Zn + Sn) | 0.77 | | 0.83 | | 0.94 | |
| Nominal Zn/Sn | 1.25 | | 1.10 | | 1.04 | |
| Lamella | I | II | I | II | I | II |
| <i>Secondary phase segregations</i> | | | | | | |
| ZnS(Se) | ✓ | ✓ | ✓ | ✓ | X | X |
| Elemental Cu | X | X | X | ✓ | X | X |
| <i>CZTSSe compositional fluctuations</i> | | | | | | |
| Less Cu-poor, Zn-rich domains | ✓ | ✓ | ✓ | ✓ | X | X |
| Vertical gradients | X | ✓ | X | X | X | X |
| Horizontal gradients | X | X | ✓ | X | X | X |
| <i>Grain boundaries</i> | | | | | | |
| Cu increased, Zn reduced, Sn unchanged | X | X | ✓ | ✓ | ✓ | ✓ |
| <i>Back contact</i> | | | | | | |
| Less Cu-poor, Zn-rich region | X | X | ✓ | ✓ | X | X |
| Mo–Cu–(S,Se) layer | ✓ | ✓ | ✓ | ✓ | ✓ | ✓ |

is formed only for composition C1 and is not observed for C2 and C3. A Mo–Cu–(S,Se) layer is formed for all compositions between the CZTSSe absorber and the Mo back contact.

These outcomes explicitly show the strong need to investigate compositional variations at the highest spatial resolution and on different regions of the absorber layer. Not only the local off-stoichiometry type of the CZTSSe influences the conversion efficiency, but also variations at nanometer scale, such as grain boundaries, which can be detrimental to the cell performance.

3. Conclusion

The spatially resolved composition and microstructure of CZTSSe solar cell absorbers with different nominal compositions and different levels of performance were investigated by combining electron and X-ray microscopies at the nanoscale. Using EDS and nano-XRF, we show the coexistence of the CZTSSe absorber material and ZnS(Se) secondary phase segregations, whose size and number increase when the synthesis conditions become Cu poorer and Zn richer, whereas they are not present when the sample preparation takes place close to stoichiometry. Furthermore, our findings demonstrate that the overall composition can be misleading, because not only the anion concentrations severely fluctuate within the CZTSSe layer, but also the local cation compositions of the absorber show significant deviations with respect to each other and with respect to the nominal composition. These local variations imply the formation of different off-stoichiometry types associated with different intrinsic point defects, which strongly affect the local electronic properties. Cu-poor and Zn-rich conditions lead to less variations of the off-stoichiometry types and to overall more beneficial A-type defects. In contrast, compositions closer to stoichiometry may exhibit much more diverse point defects and less prominent A-type defects. The conversion efficiency showed the best performance for the Cu-poorest and Zn-richest composition, due to

less variations of the off-stoichiometry types, indicating that the presence of ZnS(Se) secondary phase segregations is not the main limitation in these solar cells at the current level of performance. Moreover, the nano-XRF measurements allow to observe subtle compositional changes at the nanometer scale, revealing not only CZTSSe domains with a less Cu-poor, Zn-rich composition, but also grain boundaries with increased Cu, decreased Zn, and unchanged Sn concentration for some absorber compositions. In summary, our work opens new avenues in photovoltaics for further local compositional analysis with both nanometer resolution and elemental sensitivity using both X-ray and electron beam probes.

4. Experimental Section

Thin-Film Synthesis: The CZTSSe absorbers were fabricated by IMRA Europe using a non-pyrolitic spraying of an additive-free water-ethanol (90–10 vol%) based ink of a Cu–Zn–Sn sulfide colloid of ≈ 10 nm size primary particles, followed by a two-step annealing process. By tuning the cation composition ratio of the metal chloride salts in the mother solution, three absorber layers with different compositions were synthesized (see Table 1, Supporting Information). Details about the solar cell preparation can be found in the Supporting Information and in the reference material reported by Larramona et al.^[25,39,40]

Preparation of Cross-Sectional Lamellae: The cross-sectional lamellae were prepared out of CZTSSe/Mo/glass stacks using a focused ion beam (FIB) in an FEI Helios NanoLab 600i DualBeam system, in the same way as described by Schöppe et al.^[22] For each nominal CZTSSe composition, two lamellae were prepared at different lateral positions. In addition, a cross-sectional lamella was taken out of a homogeneous, stoichiometric, single-phase CZTSe powder grain (see Figure S1, Supporting Information) synthesized by solid-state reaction.^[19] The final thicknesses of the lamellae ranged from 170 to 340 nm.

Characterization of Cross-Sectional Lamellae: SEM and HAADF-STEM were also applied using the FEI Helios NanoLab 600i DualBeam system. The latter together with an Oxford Instruments X-Max^N detector was used to measure EDS signals taken with an electron energy of 30 kV, a current of 0.69 nA, and an acquisition time of 15 min μm^{-2} . More details about the EDS measurements can be found in the Supporting Information. Subsequently, the cation concentrations were calibrated with the values obtained from the stoichiometric CZTSe lamella. This calibration sample was probed several times during the investigation, resulting in reproducible calibration factors. Furthermore, consecutive measurements on the same spot or on different spots yield the same standard deviation of the compositional estimations, demonstrating that the stoichiometric CZTSe sample is indeed homogeneous within the experimental uncertainty of our EDS measurements. The nano-XRF acquisitions (spot analyses and mapping) were conducted at the nano-analysis beamline ID16B of the European Synchrotron Radiation Facility (ESRF) in Grenoble, France.^[41] These measurements were performed at 29.6 keV, with a focal spot size of 54×52 nm² and a step size of 50 nm, while keeping the dead time of the XRF detector below 20%. For details concerning the end station, see the Supporting Information.

Supporting Information

Supporting Information is available from the Wiley Online Library or from the author.

Acknowledgements

The authors acknowledge the ESRF for provision of synchrotron radiation facilities (experiment: MA-3564) and the valuable help of Dr. Damien

Salomon. This work was financially supported by the German Federal Ministry of Education and Research under the nano@work project (contract number: 05K16S1) and by the Deutsche Forschungsgemeinschaft (DFG, German Research Foundation) under the project number SCHN 1283/2-1. IMRA Europe acknowledges the European Commission for the funding on the Kesterite research from 2017 by the H2020 programme under the project STARCELL (H2020-NMBP-03-2016-720907). G.M.-C. acknowledges the funding by the Spanish Ministry of Innovation, Science, and Technology and the Spanish Ministry of Economy through Research Project RTI2018-097195-B-I00. Open access funding enabled and organized by Projekt DEAL.

Conflict of Interest

The authors declare no conflict of interest.

Author Contributions

The manuscript was written through contributions of all authors. All authors have given approval to the final version of the manuscript.

Keywords

defects, energy dispersive X-ray spectroscopy, kesterites, nano-XRF, thin-film photovoltaics

Received: July 13, 2020

Revised: August 13, 2020

Published online: September 22, 2020

- [1] S. Chen, A. Walsh, J.-H. Yang, X. G. Gong, L. Sun, P.-X. Yang, J.-H. Chu, S.-H. Wei, *Phys. Rev. B* **2011**, *83*, 125201.
- [2] K. Ito, N. Tatsu, *Jpn. J. Appl. Phys.* **1988**, *27*, 2094.
- [3] W. Wang, M. T. Winkler, O. Gunawan, T. Gokmen, T. K. Todorov, Y. Zhu, D. B. Mitzi, *Adv. Energy Mater.* **2014**, *4*, 1301465.
- [4] S. Giraldo, E. Saucedo, M. Neuschitzer, F. Oliva, M. Placidi, X. Alcobé, V. Izquierdo-Roca, S. Kim, H. Tampo, H. Shibata, A. Pérez-Rodríguez, P. Pistor, *Energy Environ. Sci.* **2018**, *11*, 582.
- [5] Y. S. Lee, T. Gershon, O. Gunawan, T. K. Todorov, T. Gokmen, Y. Virgus, S. Guha, *Adv. Energy Mater.* **2015**, *5*, 1401372.
- [6] K.-J. Yang, D.-H. Son, S.-J. Sung, J.-H. Sim, Y.-I. Kim, S.-N. Park, D.-H. Jeon, J. Kim, D.-K. Hwang, C.-W. Jeon, D. Nam, H. Cheong, J.-K. Kang, D.-H. Kim, *J. Mater. Chem. A* **2016**, *4*, 10151.
- [7] S. Siebentritt, S. Schorr, *Prog. Photovoltaics: Res. Appl.* **2012**, *20*, 512.
- [8] A. Kanevce, I. Repins, S.-H. Wei, *Sol. Energy Mater. Sol. Cells* **2015**, *133*, 119.
- [9] J. Just, C. M. Sutter-Fella, D. Lützenkirchen-Hecht, R. Frahm, S. Schorr, T. Unold, *Phys. Chem. Chem. Phys. PCCP* **2016**, *18*, 15988.
- [10] S. Schorr, G. Gurieva, M. Guc, M. Dimitrievska, A. Pérez-Rodríguez, V. Izquierdo-Roca, C. S. Schnorr, J. Kim, W. Jo, J. M. Merino, *J. Phys. Energy* **2020**, *2*, 12002.
- [11] M. Kumar, A. Dubey, N. Adhikari, S. Venkatesan, Q. Qiao, *Energy Environ. Sci.* **2015**, *8*, 3134.
- [12] K. Kaur, M. Sood, N. Kumar, H. H. Nazari, G. S. Gudavalli, T. P. Dhakal, M. Kumar, *Sol. Energy Mater. Sol. Cells* **2018**, *179*, 22.
- [13] P. Schöppe, G. Gurieva, S. Giraldo, G. Martínez-Criado, C. Ronning, E. Saucedo, S. Schorr, C. S. Schnorr, *Appl. Phys. Lett.* **2017**, *110*, 43901.
- [14] S. Chen, A. Walsh, X.-G. Gong, S.-H. Wei, *Adv. Mater.* **2013**, *25*, 1522.

- [15] S. Ahmed, K. B. Reuter, O. Gunawan, L. Guo, L. T. Romankiw, H. Deligianni, *Adv. Energy Mater.* **2012**, *2*, 253.
- [16] J. Márquez, M. Neuschitzer, M. Dimitrievska, R. Gunder, S. Haass, M. Werner, Y. E. Romanyuk, S. Schorr, N. M. Pearsall, I. Forbes, *Sol. Energy Mater. Sol. Cells* **2016**, *144*, 579.
- [17] X. Liu, Y. Feng, H. Cui, F. Liu, X. Hao, G. Conibeer, D. B. Mitzi, M. Green, *Prog. Photovoltaics: Res. Appl.* **2016**, *24*, 879.
- [18] S. Bourdais, C. Choné, B. Delatouche, A. Jacob, G. Larramona, C. Moisan, A. Lafond, F. Donatini, G. Rey, S. Siebentritt, A. Walsh, G. Dennler, *Adv. Energy Mater.* **2016**, *6*, 1502276.
- [19] L. E. Valle Rios, K. Neldner, G. Gurieva, S. Schorr, *J. Alloys Compd.* **2016**, *657*, 408.
- [20] G. Gurieva, L. E. Valle Rios, A. Franz, P. Whitfield, S. Schorr, *J. Appl. Phys.* **2018**, *123*, 161519.
- [21] A. Lafond, L. Choubrac, C. Guillot-Deudon, P. Deniard, S. Jobic, *Z. Anorg. Allg. Chem.* **2012**, *638*, 2571.
- [22] P. Schöppe, C. S. Schnorr, M. Oertel, A. Kusch, A. Johannes, S. Eckner, M. Burghammer, G. Martínez-Criado, U. Reislöhner, C. Ronning, *Appl. Phys. Lett.* **2015**, *106*, 13909.
- [23] J. Timo Wätjen, J. J. Scragg, M. Edoff, S. Rubino, C. Platzer-Björkman, *Appl. Phys. Lett.* **2013**, *102*, 51902.
- [24] K. Wang, B. Shin, K. B. Reuter, T. Todorov, D. B. Mitzi, S. Guha, *Appl. Phys. Lett.* **2011**, *98*, 51912.
- [25] G. Larramona, S. Bourdais, A. Jacob, C. Choné, T. Muto, Y. Cuccaro, B. Delatouche, C. Moisan, D. Péré, G. Dennler, *J. Phys. Chem. Lett.* **2014**, *5*, 3763.
- [26] J. Just, D. Lützenkirchen-Hecht, R. Frahm, S. Schorr, T. Unold, *Appl. Phys. Lett.* **2011**, *99*, 262105.
- [27] K. Woo, Y. Kim, W. Yang, K. Kim, I. Kim, Y. Oh, J. Y. Kim, J. Moon, *Sci. Rep.* **2013**, *3*, 3069.
- [28] S. Kasap, *Springer Handbook of Electronic and Photonic Materials*, Springer, New York, NY **2006**.
- [29] K. E. Roelofs, Q. Guo, S. Subramoney, J. V. Caspar, *J. Mater. Chem. A* **2014**, *2*, 13464.
- [30] M. Ritzer, S. Schönherr, P. Schöppe, W. Wisniewski, S. Giraldo, G. Gurieva, A. Johannes, C. T. Plass, K. Ritter, G. Martínez-Criado, S. Schorr, E. Saucedo, C. Ronning, C. S. Schnorr, *ACS Appl. Energy Mater.* **2020**, *3*, 558.
- [31] P. Schöppe, S. Schönherr, P. Jackson, R. Wuerz, W. Wisniewski, M. Ritzer, M. Zapf, A. Johannes, C. S. Schnorr, C. Ronning, *ACS Appl. Mater. Interfaces* **2018**, *10*, 40592.
- [32] P. Schöppe, S. Schönherr, M. Chugh, H. Mirhosseini, P. Jackson, R. Wuerz, M. Ritzer, A. Johannes, G. Martínez-Criado, W. Wisniewski, T. Schwarz, C. T. Plass, M. Hafermann, T. D. Kühne, C. S. Schnorr, C. Ronning, *Nano Energy* **2020**, *71*, 104622.
- [33] V. A. Solé, E. Papillon, M. Cotte, P. Walter, J. Susini, *Spectrochim. Acta Part B* **2007**, *62*, 63.
- [34] S. Bag, O. Gunawan, T. Gokmen, Y. Zhu, T. K. Todorov, D. B. Mitzi, *Energy Environ. Sci.* **2012**, *5*, 7060.
- [35] T. Schwarz, O. Cojocaru-Mirédin, P. Choi, M. Mousel, A. Redinger, S. Siebentritt, D. Raabe, *J. Appl. Phys.* **2015**, *118*, 95302.
- [36] N. A. Kattan, I. J. Griffiths, D. Cherns, D. J. Fermín, *Nanoscale* **2016**, *8*, 14369.
- [37] K. Kaur, K. Arora, B. Behzad, Q. Qiao, M. Kumar, *Nanotechnology* **2019**, *30*, 65706.
- [38] L. Guo, Y. Zhu, O. Gunawan, T. Gokmen, V. R. Deline, S. Ahmed, L. T. Romankiw, H. Deligianni, *Prog. Photovoltaics: Res. Appl.* **2014**, *22*, 58.
- [39] G. Larramona, S. Bourdais, A. Jacob, C. Choné, T. Muto, Y. Cuccaro, B. Delatouche, C. Moisan, D. Péré, G. Dennler, *RSC Adv.* **2014**, *4*, 14655.
- [40] G. Larramona, S. Levchenko, S. Bourdais, A. Jacob, C. Choné, B. Delatouche, C. Moisan, J. Just, T. Unold, G. Dennler, *Adv. Energy Mater.* **2015**, *5*, 1501404.
- [41] G. Martínez-Criado, J. Villanova, R. Tucoulou, D. Salomon, J.-P. Suuronen, S. Labouré, C. Guilloud, V. Valls, R. Barrett, E. Gagliardini, Y. Dabin, R. Baker, S. Bohic, C. Cohen, J. Morse, *J. Synchrotron Radiat.* **2016**, *23*, 344.